



Cite this: *New J. Chem.*, 2023, 47, 21924

Biocompatible fluorescent europium(III) magnetic nanoparticles†

Inês J. Marques,^a Pedro D. Vaz,^b Ana V. Girão,^d Mariela M. Nolasco^c and Carla D. Nunes[✉]

Silica-coated Iron oxide ($\text{Fe}_3\text{O}_4@\text{SiO}_2\text{-NP}$) and silica ($\text{SiO}_2\text{-NP}$) nanoparticles were prepared and derivatized with a Eu(III) complex to yield magneto-fluorescent ($\text{Fe}_3\text{O}_4@\text{SiO}_2\text{-NP:C2}$) and fluorescent ($\text{SiO}_2\text{-NP:C2}$) nanomaterials that could work as possible biosensors. The $\text{Fe}_3\text{O}_4\text{-NP}$ core is inactive, although it contains an important property, magnetism, allowing particles to be directed to where they are needed. The $\text{Fe}_3\text{O}_4@\text{SiO}_2\text{-NP:C2}$ and $\text{SiO}_2\text{-NP:C2}$ (without magnetism) acted as fluorescent probes by means of an anchored europium (Eu) complex, which was used as fluorescence promoter, holding condensed aromatic ring as neutral ligands working as antenna – phenanthroline – that enhanced the fluorescence. The results showed that the cytotoxicity of the samples was almost inexistent, while fluorescent character was maintained unaltered in cellular medium for all the studied materials. This work provides new understandings through these nanomaterials for their potential application in imaging, representing a less toxic, more economically viable and sustainable solution, compared to existing ones.

Received 22nd October 2023,
Accepted 7th November 2023

DOI: 10.1039/d3nj04897g

rsc.li/njc

Introduction

The search for new and promising contrast agents for multi-modal clinical and preclinical imaging applications attracts much interest.¹ The contrast mechanism depends on the choice of imaging modality, which itself is determined by the clinical problem and accessibility for imaging. For example, carrier moieties such as nanoparticles (liposomes or emulsions), dendrimers, viral constructs, or various polymers can be loaded with imaging agents such as paramagnetic or super-paramagnetic metals, fluorophores, or radionuclides to enable detection.^{2,3} Iron is an essential element and, thus, a life without iron would not be possible. However, overload of iron is also hazardous since it can increase reactive oxygen species (ROS) production *via* Fenton and Haber–Weiss reactions.⁴

Fe_3O_4 nanoparticles are the most promising type of magnetic nanoparticles and have already been approved by FDA

(*i.e.* Feridex I.V.[®]) for usage in liver imaging.⁵ The chemical and physical properties of the iron oxide nanoparticles play an important role in their usage. By controlling and adjusting the particle core size, shape, bio-distribution and magnetic properties, one can meet specific parameters necessary for a variety of applications.⁶ Since the magnetic nanoparticles obey the Coulomb's law, they can be guided to a specific target site by means of an external magnetic field, making them applicable in the transportation and delivery of molecular markers and various drugs. It can be also beneficial for the use as contrast agents in magnetic resonance imaging (MRI).^{7–9}

Clinical trials suggest that functionalization of nanoparticles with specific recognition make them multifunctional and they can show higher efficiency, while simultaneously reduce the side effects due to the localization properties of the target tumor and the activated cellular uptake.¹⁰

In addition, the design of SiO_2 nanoparticles (NPs) as a proof of concept to act as attractive bioprobes in both biological and living systems, was also envisaged, due to their good biocompatibility, intrinsic low toxicity, and easy excretion from those systems.^{11–14} Silicon is the most abundant element (27.2%) in the Earth's crust after oxygen (45.5%),¹⁵ since its chemical and physical characteristics allow silicon oxide to be used in a variety of industries. Among these, biomedical applications attract great attention and grow faster, and it can be employed as dietary supplements, implants, dental fillers or contact lenses.¹⁶ The fundamental characteristics of silicon dioxide (silica)-based nanoparticles, such as size, optical properties, high surface area, low density, adsorption and encapsulation

^a Institute of Molecular Sciences, Centro de Química Estrutural – FCUL, Departamento de Química e Bioquímica, Faculdade de Ciências da Universidade de Lisboa, 1749-016 Lisboa, Portugal. E-mail: cmunes@fc.ul.pt; Fax: +351 217500088; Tel: +351 217500000 (528536)

^b Champalimaud Centre for the Unknown, Champalimaud Foundation, Av. Brasília, 1400-038 Lisboa, Portugal

^c Chemistry Department and CICECO, University of Aveiro, 3810-193 Aveiro, Portugal

^d Department of Materials and Ceramics Engineering, CICECO, University of Aveiro, 3810-193 Aveiro, Portugal

† Electronic supplementary information (ESI) available. See DOI: <https://doi.org/10.1039/d3nj04897g>



capacity, biocompatibility and low toxicity, make them an especially attractive inert solid in diverse biomedical applications.¹⁷

NPs when doped with appropriate dye molecules become intensely luminescent materials capable of signaling a biological target. Bioconjugated, fluorescent and magnetic nanoparticles have been developed for ultrasensitive bioassays (e.g. detection of bacteria).¹⁸ Magnetic iron oxide nanoparticles exhibiting magnetic moments in the vicinity of an external magnetic field, have attracted increasing interest to be widely explored in life sciences.¹⁹ Since they exhibit attractive characteristics, and easy surface-functionalization, they are emerging as attractive nanomaterials for bioprobes.^{2,20,21}

The limited optical qualities of organic dyes (weak photostability) and quantum dots (potential cytotoxicity, blinking of fluorescence and complex functionalization strategies) often limit their imaging possibilities and demand the development of better bioprobes.^{22,23} The use of lanthanide(III) ions as bioprobes is apparently restricted, due to their low molar-absorption coefficients and UV excitation wavelengths.²⁴ However, this limitation can be minimized when they are coordinated with suitable ligands.

The development of europium (Eu³⁺) antenna complexes transforms them into attractive molecules circumventing the poor water solubility and fluorescence quenching. To avoid this, one possibility is incorporating them into nanoparticles, which can provide better water dispersibility. In the last years research in the development of luminescent nanoparticles, whose optical properties and biocompatibility are promising for various biological applications, by incorporating light-excitable Eu³⁺ complexes raised exponentially.^{25–29}

The covalent linking of dye molecules in nanomaterials reduces the risk of the dyes being leached out when compared with impregnation and doping methods.^{20,30} Additionally, it improves the homogeneity and allows higher loading.

The strategy was to combine the potential of lanthanide complexes with the properties of the NPs, thus resulting in two forms of bioprobes used in bioscience, such as in MRI bioprobes and as a carrier for drugs.³¹

A probe that combines fluorescent and magnetic moment solves both the depth of resolution imaging,³² and provides a diagnostic tool for studies *in vitro* and *in vivo*, which leads to an improvement in the visualization of biological materials and greater credibility of the data collected. These bimodal probes in biological labeling are explored in photodynamic therapeutic interventions targeted to tumors and drug transporters.³³ The bimodal probes with high performance and good biocompatibility have aroused the great interest of researchers.³⁴

In this work, iron-oxide and silica nanoparticles were synthesized, and subsequently functionalized with an Eu³⁺ complex with 1,10-phenanthroline ligand to be tested as bioprobes.

Materials and methods

Reagents were obtained from Sigma-Aldrich and VWR (Avantor) and used as received. Commercial grade solvent, ethanol, was

dried and deoxygenated by standard procedures (CaO), distilled under nitrogen, and kept over 4 Å molecular sieves. Deionized water (Milli-Q) was high purity grade with a conductivity of 18.2 MΩ·cm. All materials and complexes were synthesized under nitrogen, using Schlenk techniques.

Adherent cells from *Homo sapiens cervix carcinoma*, HeLa (ATCC CCL-2), and lung carcinoma, A549 (ATCC CCL185), were purchased from American Type Culture Collection (Manassas, VA, USA). RPMI 1640 and DMEM media, heat-inactivated fetal bovine serum (FBS), penicillin and streptomycin solution, trypsin, 1× phosphate buffer solution (PBS) and MTT [3-(4,5-dimethylthiazol-2-yl)-2,5-diphenyltetrazolium bromide] salts were obtained from Thermo Fischer Scientific (Waltham, MA, USA).

Synthesis of the precursor europium complex (C1)

1,10-Phenanthroline (0.360 g, 2 mmol) was dissolved in ethanol (10 mL) at room temperature, and EuCl₃·6H₂O (0.366 g, 1 mmol) in Milli-Q water (10 mL) at 323 K. Then, the latter solution was added dropwise over the phenanthroline ethanolic solution. The reaction was maintained at 323 K, under stirring, for approximately 2 h. At the end of the reaction the solvent was evaporated to dryness under vacuum and the residue washed with ethanol to remove any unreacted ligand. Finally, it was dried under vacuum at 323 K for several hours.

Synthesis of europium complex (C2)

3-Aminopropyltrimethoxysilane (109 μL, 0.63 mmol) was added to an ethanol (10 mL) solution containing the synthesized precursor Eu complex (C1; 0.4 g, 0.63 mmol). The mixture was stirred overnight (14 h) at room temperature (298 K). In the end, the solution was evaporated to dryness and the resulting product was dried under vacuum for several hours.

Elemental analysis calcd (%) for C₃₀H₃₃N₅O₃Cl₃SiEu: Eu, 19.04; C, 45.15; H, 4.17; N, 8.78. Found (%): Eu, 18.99; C, 45.32; H, 4.32; N, 8.74.

Synthesis of iron oxide nanoparticles (Fe₃O₄-NP)

The synthesis followed a literature protocol.³⁵ Ferrous chloride (FeCl₂, 2.5 g) and ferric chloride (FeCl₃, 5 g) were added at room temperature under stirring to nitrogen purged 2-propanol (200 mL) resulting in a yellowish orange reaction mixture. Stirring was kept for 15 min, and then the temperature of the solution was raised to 353 K and 100 mL of concentrated (25%) ammonium hydroxide (NH₄OH) were slowly added. The color of the solution turned dark brown, and the stirring continued for more 2 h. The obtained magnetic nanoparticles were protected by the addition of 10 mM of oleic acid in 300 mL methanol. Then they were separated from the solution by centrifugation (10 min, 3000 rpm) and washed with methanol three times.

Synthesis of silica-coated iron oxide nanoparticles (Fe₃O₄@SiO₂-NP)

Coating of the iron oxide nanoparticles with a silica shell was done according to a published procedure as well.³⁶ Two solutions were prepared. Solution A was prepared by dispersing the



previously synthesized $\text{Fe}_3\text{O}_4\text{-NP}$ (1 g) in a mixture of absolute ethanol (100 mL), distilled water (60 mL), and aqueous ammonia (0.6 mL) in a three-neck flask under ultrasonic dispersion for 1 h at 298 K. Solution B, tetraethylorthosilicate (TEOS) (16.67 mL) was diluted in absolute ethanol (40 mL) under mechanical stirring for 10 min. Then, solution B was slowly added to solution A at a rate of 0.5 mL min^{-1} . The resulting reaction mixture was ultrasonicated for 12 h at room temperature (293–298 K). When the reaction was finished, the obtained coated Fe-NPs were centrifuged (10 min, 3000 rpm) and washed with distilled water and ethanol repeatedly for three times with each solvent. Finally, the purified product Fe@Si-NP was dried in a vacuum oven at 333 K for 4 h.

Synthesis of silica nanoparticles ($\text{SiO}_2\text{-NP}$)

Synthesis of the nanoparticles was based on a published procedure.³⁷ Silica nanoparticles ($\text{SiO}_2\text{-NP}$) were synthesized by adding TEOS (6 mL), ammonia (30 mL), and 10 mL of Milli-Q water to a given volume of absolute methanol, with the final volume of the mixture being 500 mL. The reaction mixture was stirred at *ca.* 400 rpm for 12 h at room temperature (298 K). The $\text{SiO}_2\text{-NP}$ were washed three times with ethanol by centrifugation-redispersion at 10000 rpm.

Synthesis of iron nanoparticles with europium complex ($\text{Fe}_3\text{O}_4\text{@Si-NP:C2}$)

The silica-coated iron oxide nanoparticles ($\text{Fe}_3\text{O}_4\text{@SiO}_2\text{-NP}$) were functionalized with Eu complex by dissolving the Eu complex (C2; 0.44 g, 0.55 mmol) in absolute ethanol (10 mL) under stirring for 15 min, at 323 K. Then this solution was added, dropwise, to an aqueous suspension (15 mL) of $\text{Fe}_3\text{O}_4\text{@SiO}_2\text{-NP}$ (0.35 g) and left under stirring at reflux for 24 h. At the end, the obtained material ($\text{Fe}_3\text{O}_4\text{@SiO}_2\text{-NP:C2}$) was centrifuged (10 min, 3000 rpm) and washed with distilled water and ethanol repeatedly for three times with each solvent. Finally, the purified product $\text{Fe}_3\text{O}_4\text{@SiO}_2\text{-NP:C2}$ was dried in a vacuum oven at 333 K for 4 h.

Elemental analysis (found, %): Eu, 3.71; C, 7.98; H, 1.30; N, 1.74.

Synthesis of silica nanoparticles with europium complex ($\text{SiO}_2\text{-NP:C2}$)

The adopted procedure was similar to the one reported above for the synthesis of $\text{Fe}_3\text{O}_4\text{@SiO}_2\text{-NP:C2}$.

Elemental analysis (found, %): Eu, 3.15; C, 6.83; H, 1.38; N, 1.48.

Spectroscopic and structural characterization

All materials and complexes were characterized by powder XRD using $\text{CuK}\alpha$ radiation (Pw 3050/60 X'Pert PRO X-ray, Philips Analytical), FTIR (Nicolet 6700 spectrometer, Thermo Scientific), fluorescence (Fluorolog-3 Model FL3-2T Horiba) with double excitation using a Xenon lamp (450 W) as source.

The morphology and the diameter of the NP was measured by TEM microscope (H-8100, Hitachi) with a LaB_6 filament, at an accelerating voltage of 200 kV and by FEG-SEM microscope

field emission electron microscope at an accelerating voltage of 200 kV, (JSM-7001F, JEOL) at Microlab (Instituto Superior Técnico, Portugal). Measurements were also conducted using a TEM Jeol 2200FS, operated at 200 kV with energy dispersive spectroscopy (EDS) system (Oxford Instruments). The samples were prepared by dropping a dispersion of the powder in isopropanol onto a copper grid with a holey carbon film and left to dry in air.

The loading of Eu complex (C2) at the surface of the nanoparticles was calculated by Thermogravimetric Analysis (TG analyser 7, PerkinElmer) under N_2 and He gas, and by Elemental Analysis (Vigo, Spain). UV-Vis was measured on a Shimadzu UV2450, fluorescence studies using a microplate reader (Spectra MAX Gemini EM, Molecular Devices) and solid fluorescence studies on a JASCO spectrofluorometer type FP-8300.

The DLS and ζ potential (pH 7) measurements were performed using a Litesizer 500 from Anton Paar. Measurements were performed at 298 K and the results presented as number-based distributions.

Cell culture (HeLa and A549) and cell viability assay

For cell viability assay and fluorescence studies, cervical (HeLa) and alveolar (A549) adenocarcinoma cell lines were cultured following reported methods.³⁸ RPMI 1640 without L-Glutamine and DMEM without L-Glutamine were used as growth media, respectively, for the cell lines. Both media were supplemented with 10% fetal bovine serum (FBS), 1% penicillin-streptomycin (200 U mL^{-1} PEN-STREP) and 1% L-Glutamine (2 mM). Cell culture was performed at 310 K under a 95% air/5% CO_2 humidified atmosphere condition. For cell viability assay and fluorescence studies cells were grown in 96-well plates.

Cytotoxic effects of the nanoparticles were tested with MTT [3-(4,5-dimethylthiazol-2-yl)-2,5-diphenyltetrazolium bromide] assay. Approximately 3×10^5 cells were seeded on each well of 96-well plates and incubated for 48 h. Later, spent medium was removed and various concentrations of the nanoparticles (8 different concentrations) were added and incubated for another 48 h. After exchanging the culture medium with 100 μL of the MTT solution (0.5 mg mL^{-1} dissolved MTT in medium), the plates were incubated for 2 h. Finally, 100 μL of DMSO (dimethyl sulfoxide) were added and the absorbance at 570 nm measured using plate reader.

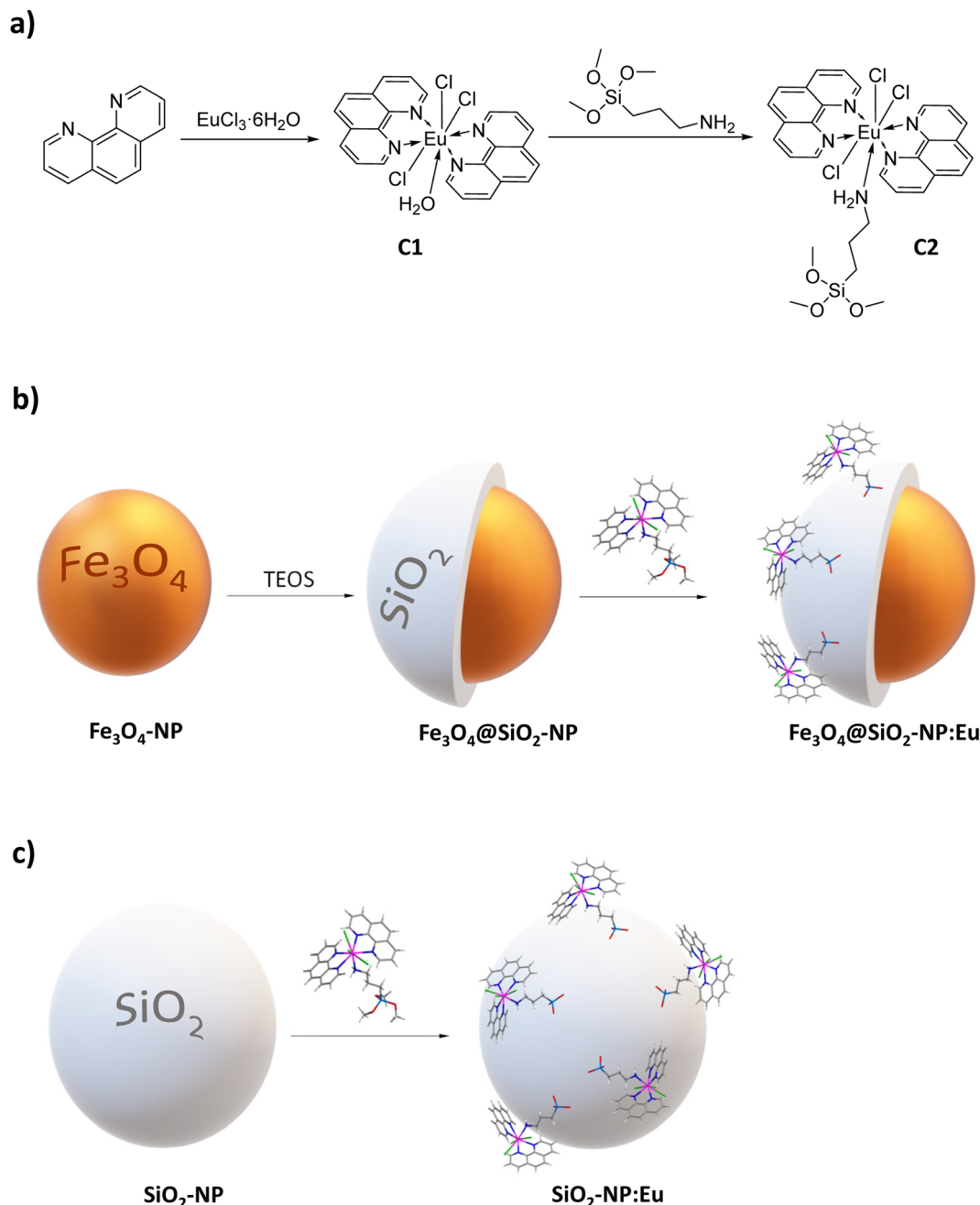
Results and discussion

The overall synthetic procedures carried out within the framework of the present research are shown in Scheme 1, comprising the synthesis of the Eu complexes, C1 and C2, and subsequent engineering of both the $\text{Fe}_3\text{O}_4\text{@SiO}_2\text{-NP:C2}$ and $\text{SiO}_2\text{-NP:C2}$ nanomaterials.

Synthesis and characterization of the europium complexes

The synthesis of the europium complex C2 was conducted promoting the reaction of $\text{EuCl}_3 \cdot 6\text{H}_2\text{O}$ with phenanthroline (*phen*) and 3-aminopropyltrimethoxysilane (*aptms*), stepwise,





Scheme 1 Experimental routes for synthesis of the C1 and C2 Eu complexes (a), $\text{Fe}_3\text{O}_4@\text{SiO}_2\text{-NP:C2}$ (b) and $\text{SiO}_2\text{-NP:C2}$ (c) nanomaterials.

allowing to prepare the fluorescent moiety for subsequent grafting into the surface of iron oxide and silica nanoparticles. The synthesis of the C2 was accomplished as shown in Scheme 1a.

The X-ray diffraction powder patterns were measured for both complexes (Fig. 1). For complex C1, the corresponding powder pattern was found to match very closely that reported for the $\text{EuCl}_3(\text{H}_2\text{O})(\text{phen})_2$ similar system as reported by Lhoste (REFCODE 806463).³⁹ Complex C2 also showed a diffraction pattern similar to that obtained for C1, but with slight differences as expected. The thermogravimetric analysis (TGA) of C1 complex (Fig. S1, ESI†) displayed a very well-defined three step

profile matching that found in the literature as well.³⁹ The first step, up to 400 K, is due to the coordinated water and some residual solvent. The following events till 800 K could be due to the stepwise release of the *phen* ligands and some of the chloride, as reported earlier.³⁹ The TGA of C2 (Fig. S1, ESI†) was found to have a less differentiated profile with an almost continuous mass loss from room temperature till 700 K. In this case the loss of the *phen*, *apts* and chloride ligands is not so defined. It should also be mentioned that the residual mass is higher than that measured for C1. A plausible explanation for this is the fact that the final mass may be a mixed oxide of silica and europium.



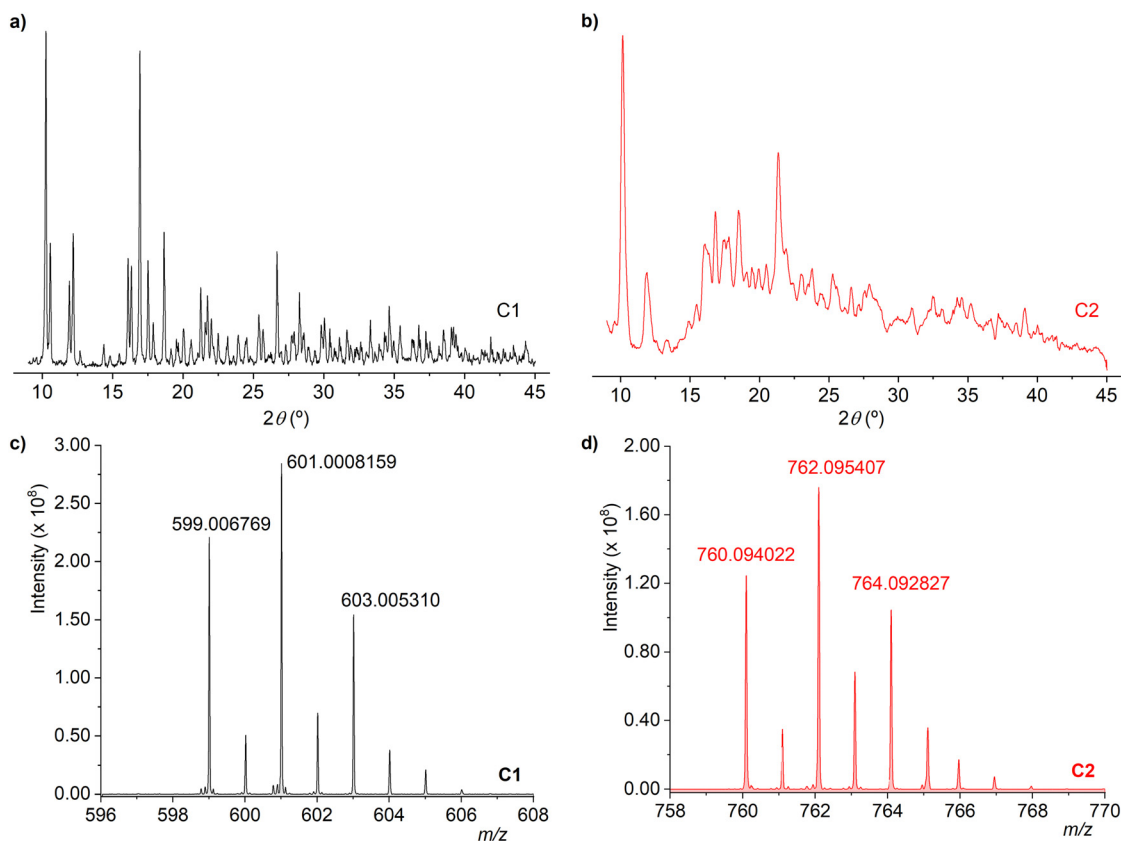


Fig. 1 X-ray powder patterns of C1 (a) and C2 (b) complexes. High resolution mass spectrometry (HR-MS) isotope patterns of $[M - Cl]^+$ ions for both C1 (c) and C2 (d) complexes.

The synthesis of both Eu complexes and their corresponding proposed structures (as shown in Scheme 1a) was confirmed by high-resolution mass spectra (HR-MS) using electrospray ionization (ESI). HR-MS allowed analysis of both the molecular mass and the associated isotopic patterns to be confirmed as formulated (Scheme 1a). Both complexes were detected at m/z values corresponding to the formulated complexes in the form of their molecular ions following the loss of a Cl ligand yielding the corresponding positively monocharged ions. Therefore, both complexes were successfully detected as the expected m/z values in the form of $[M - Cl]^+$ ions, Table 1. Detection of the molecular ions was accomplished with excellent agreement between the measured and expected m/z values as confirmed by relatively low errors (Table 1).

Additionally, the isotopic patterns found for the measured $[M - Cl]^+$ ions were found to match the expected formulations as shown in Fig. 1.

Collision induced dissociation (CID) experiments carried out with argon resulted in the loss of specific fragments from

the original complexes. In the case of C1, CID afforded the loss of one *phen* ligand, formulated as $[C1-Cl-phen]^+$, detected at $m/z = 420.937583$ showing an error of -0.3 ppm relative to the expected ion at $m/z = 420.937700$.

On the other hand, fragmentation of C2 under CID conditions yielded two ions at $m/z = 582.995997$ and at $m/z = 402.927462$, with errors of $+0.2$ and $+0.8$ ppm to the corresponding expected m/z values, respectively. The former was due to the loss of amino siloxane (*aptsms*) ligand, formulated as $[C2-Cl-aptsms]^+$, while the latter was due to the loss of both the *aptsms* and one *phen* ligand being formulated as $[C2-Cl-aptsms-phen]^+$.

The infrared spectrum of the synthesized C2 complex showed typical bands of the N-H, C=N and C=C bonds, between $3500-3300\text{ cm}^{-1}$ ($\nu\text{N-H}$), 1620 cm^{-1} ($\nu\text{C=N}$) and $1600-1500\text{ cm}^{-1}$ ($\nu\text{C=C}_{\text{aromatic}}$) as well as the characteristic bands of europium 1636 , 1464 and 696 cm^{-1} . There was also the presence of a band at 1085 cm^{-1} , assigned to the

Table 1 Calculated and experimental molecular weight of synthesized complexes detected in HR-MS experiments

Complex	Ion formula ^a	Calculated MW	Experimental MW	Error (ppm)
C1	$[\text{Eu}(\text{C}_{12}\text{H}_8\text{N}_2)_2(\text{H}_2\text{O})\text{Cl}_2]^+$	601.006448	601.008159	+2.8
C2	$[\text{Eu}(\text{C}_{12}\text{H}_8\text{N}_2)_2(\text{C}_6\text{H}_{17}\text{NO}_3\text{Si})\text{Cl}_2]^+$	762.093654	762.095407	+2.3

^a All ions detected as $[M-Cl]^+$ ions after loss of a chloride ligand according to the formulas proposed.



$\nu_{\text{asym}}\text{Si-O-Si}$, confirming the presence of the 3-aminopropyltrimethoxysilane ligand. In addition, a sharp band at 1590 cm^{-1} , could be assigned to the bending mode of the primary amine in the 3-aminopropyltrimethoxysilane ligand. This was found to be proof of coordination to the Eu core since it was red-shifted from its uncoordinated position (1600 cm^{-1}).

Synthesis and characterization of the iron oxide nanoparticles

The magnetic iron nanoparticles ($\text{Fe}_3\text{O}_4\text{-NP}$) were synthesized following a co-precipitation method, using iron(II) and iron(III) chloride and ammonia as agent to promote the hydrolysis.³⁵ Afterwards, the obtained material ($\text{Fe}_3\text{O}_4\text{-NP}$) was coated with a silica layer using tetraethylorthosilicate (TEOS) as silica source,³⁶ which were designated as $\text{Fe}_3\text{O}_4@\text{SiO}_2\text{-NP}$. The layer of silica enabled surface grafting, since the Si-OH groups can react with siloxane moiety of the Eu complex. The synthetic route is shown in Scheme 1b.

The surface functionalization of the $\text{Fe}_3\text{O}_4@\text{SiO}_2\text{-NP}$ was carried out with the pendent arm of the C2 complex originating the $\text{Fe}_3\text{O}_4@\text{SiO}_2\text{-NP:C2}$ derivatized magnetic nanoparticles.

All obtained materials, $\text{Fe}_3\text{O}_4\text{-NP}$, $\text{Fe}_3\text{O}_4@\text{SiO}_2\text{-NP}$ and $\text{Fe}_3\text{O}_4@\text{SiO}_2\text{-NP:C2}$ were characterized by FTIR (Fig. S2a, ESI†) in order to understand if the reaction occurred, by the analysis of the vibrational modes of the different functional groups.

By comparing the spectra of the iron nanoparticles ($\text{Fe}_3\text{O}_4\text{-NP}$, not shown) and coated with silica ($\text{Fe}_3\text{O}_4@\text{SiO}_2\text{-NP}$) both have a band assigned to $\nu\text{Fe-O}$ modes (755 cm^{-1}) while the $\text{Fe}_3\text{O}_4@\text{SiO}_2\text{-NP}$ feature a band assigned to $\nu\text{Si-O-Si}$ (1060 cm^{-1}) mode due to their coating with silica. After reacting with the previously synthesized Eu complex, C2, it was possible to observe the presence of some characteristic bands corresponding to the functional groups of the C2 complex, as is the case of $\nu\text{N-H}$ ($3500\text{--}3300\text{ cm}^{-1}$) mode of the terminal amine moiety, the $\nu\text{C=N}$ ($1680\text{--}1610\text{ cm}^{-1}$) and $\nu\text{C=C}_{\text{aromatic}}$ ($1600\text{--}1500\text{ cm}^{-1}$) modes of the aromatic *phen* ligands.

Elemental analysis showed that the Eu content was 3.71% in the $\text{Fe}_3\text{O}_4@\text{SiO}_2\text{-NP:C2}$ nanomaterial, corresponding to a C2 complex loading of 0.24 mmol g^{-1} .

The X-ray powder diffractograms of the pristine, shelled and derivatized magnetic iron oxide nanoparticles showed no major changes in the diffraction peaks profiles, as shown in Fig. 2a.

All diffractograms exhibited a set of six main diffraction peaks that correspond to the typical magnetite structure (Fe_3O_4). A small impurity was also detected due to oxidized magnetite; although Raman spectroscopy can yield the qualitative identification of iron oxide phases,⁴⁰ ^{57}Fe Mössbauer spectroscopy, which assesses both qualitative and quantitative iron oxide phases unequivocally, has already provided clear evidence that these synthesized iron oxide nanoparticles are almost pure magnetite (Fe_3O_4 , ICDD 01-080-6402) with just a slight impurity (ca. 3%).⁴¹

The core structure was preserved across both the silica shelling procedure ($\text{Fe}_3\text{O}_4@\text{SiO}_2\text{-NP}$) and functionalization of the nanoparticles with Eu complex ($\text{Fe}_3\text{O}_4@\text{SiO}_2\text{-NP:C2}$) as confirmed by the X-ray diffraction (XRD) powder patterns. Both diffractograms of $\text{Fe}_3\text{O}_4@\text{SiO}_2\text{-NP}$ and $\text{Fe}_3\text{O}_4@\text{SiO}_2\text{-NP:C2}$

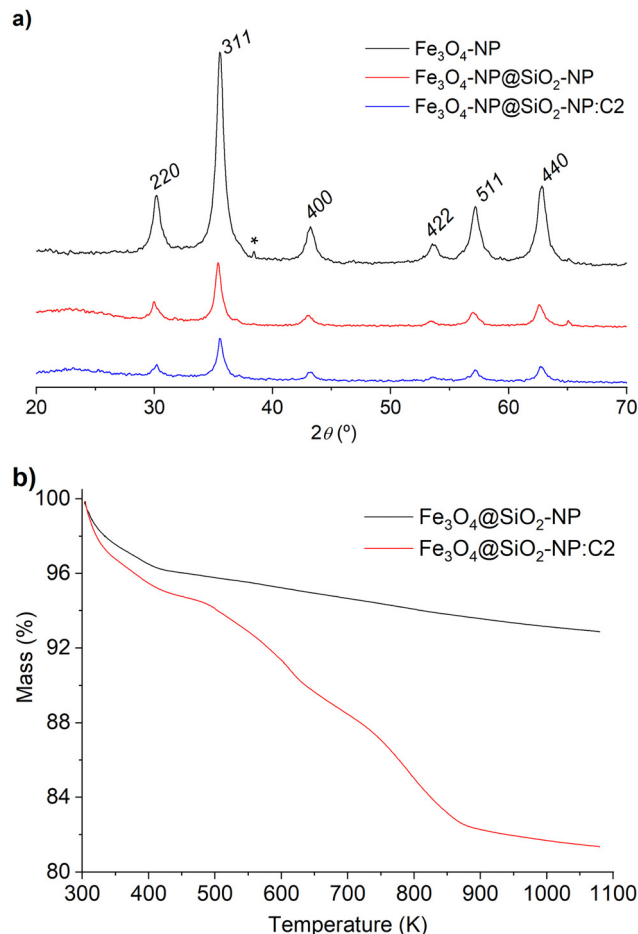


Fig. 2 X-Ray powder diffraction patterns of all steps of the synthetic pathway of iron oxide nanoparticles (a) and thermogravimetric analysis (TGA) of $\text{Fe}_3\text{O}_4@\text{SiO}_2\text{-NP}$ and $\text{Fe}_3\text{O}_4@\text{SiO}_2\text{-NP:C2}$ (b). In (a) the * denotes a slight impurity (ca. 3%) due to oxidized magnetite.⁴¹

nanomaterials evidenced the presence of the SiO_2 shell by the presence of a broad diffraction feature centered at $2\theta = 23^\circ$ (Fig. 2a). In addition, the apparent signal attenuation of the diffractogram intensity is not due to a loss of crystallinity. Instead, it is due to the presence of Si (in $\text{Fe}_3\text{O}_4@\text{SiO}_2\text{-NP}$ and $\text{Fe}_3\text{O}_4@\text{SiO}_2\text{-NP:C2}$) and Eu (in $\text{Fe}_3\text{O}_4@\text{SiO}_2\text{-NP:C2}$), which scatter the radiation as well. This effect is well documented in the literature.⁴² Moreover, it can be concluded that after the reactions the diffractograms displayed the same reflections, showing that the magnetite structure was maintained during those processes.

Thermogravimetric analysis (TGA) was accomplished, allowing to determine the loss of mass and calculate the amount of Eu complex that was grafted at the surface of $\text{Fe}_3\text{O}_4@\text{SiO}_2\text{-NP:C2}$ (Fig. 2b).

By observing the TGA profile of $\text{Fe}_3\text{O}_4@\text{SiO}_2\text{-NP}$ there was a loss of 3.9% weight, noticed in the region between 300 and 430 K, due to physisorbed water molecules. Above 430 K, the thermal profile of the $\text{Fe}_3\text{O}_4@\text{SiO}_2\text{-NP}$ nanomaterial showed an almost linear mass loss rate amounting to 3.2%. This mass loss is mostly due to strongly bound water molecules and to some dehydroxylation processes at the surface.



In the case of the $\text{Fe}_3\text{O}_4@\text{SiO}_2\text{-NP:C2}$ counterpart, the first mass loss occurred across a slightly wider temperature range (300–460 K) and reaching 5.3%, which indicated a higher degree of adsorbed moisture. Above 460 K, the thermal degradation $\text{Fe}_3\text{O}_4@\text{SiO}_2\text{-NP:C2}$ occurred through two steps. The first one was observed between 460 and 640 K corresponding to a mass loss of 4.7%, while the second degradation step was observed between 640 and 880 K, with a loss of 7.6%. Both steps are due to decomposition of the C2 complex grafted at the surface of $\text{Fe}_3\text{O}_4@\text{SiO}_2\text{-NP:C2}$. Assuming the combined mass loss of both steps to be originated on the C2 complex, this meant that the Eu complex was 12.3% w/w, although accounting for the 3.2% mass loss due to dehydroxilation yielded a net complex mass loss of 8.9%, assumed to be exclusively due to

the Eu complex. This corresponded to a loading of 0.16 mmol g^{-1} . Results from elemental analysis showed an Eu content of 3.71%, yielding a complex loading of 0.24 mmol g^{-1} , showing a good agreement between both values. The lower value obtained from TGA is due to the fact that Eu atoms will be part of the final mass, most probably in the form of an oxide and, therefore, the loading value is not as accurate as that obtained from the Eu elemental analysis.

Scanning and transmission electron microscopy techniques (SEM and TEM, respectively) were used to characterize the morphology of both $\text{Fe}_3\text{O}_4@\text{SiO}_2\text{-NP}$ and $\text{Fe}_3\text{O}_4@\text{SiO}_2\text{-NP:C2}$ magnetic iron oxide nanoparticles.

The SEM images of both nanomaterials, Fig. 3a and b, showed that the nanoparticles were spherical in shape and

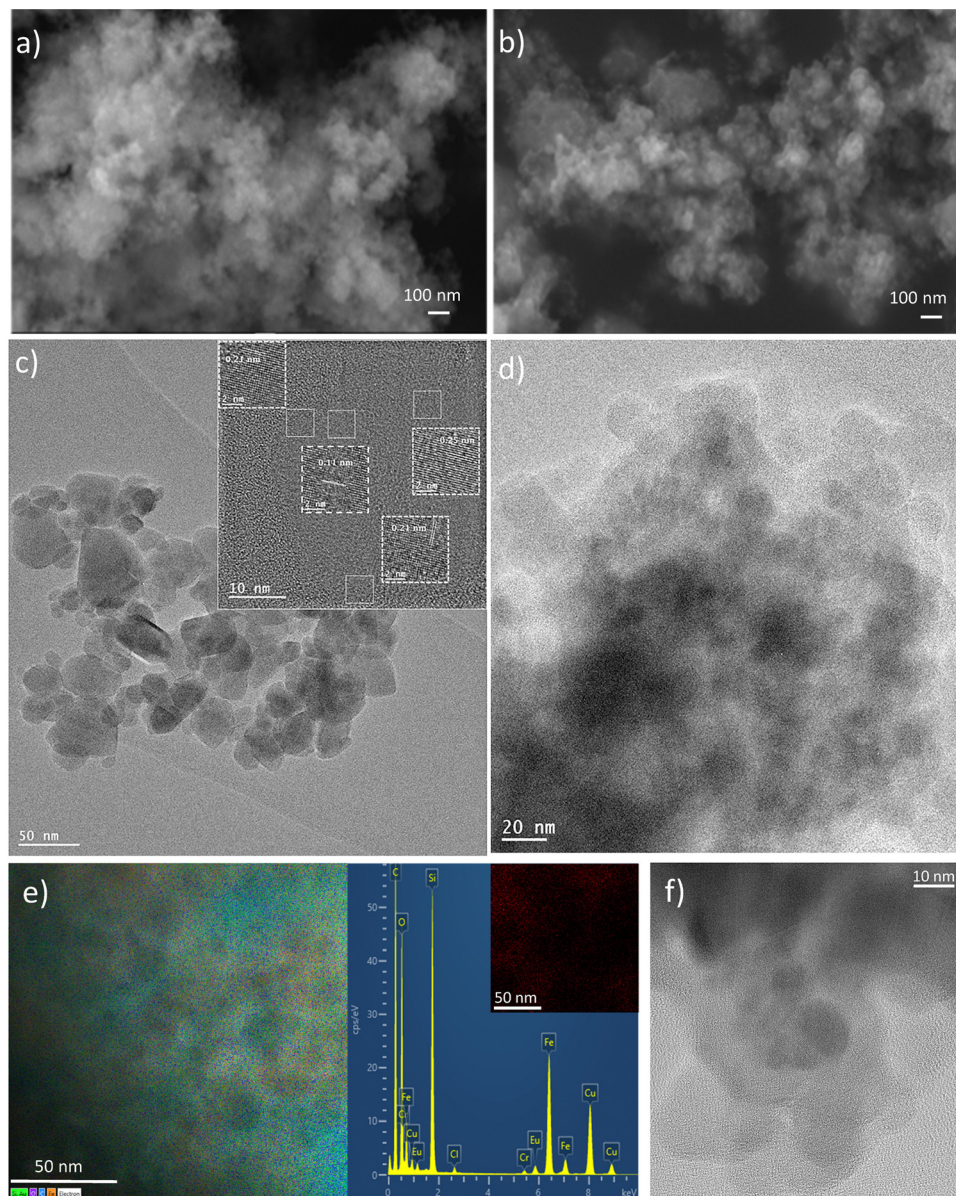


Fig. 3 The top row shows SEM images of $\text{Fe}_3\text{O}_4@\text{SiO}_2\text{-NP}$ (a) and $\text{Fe}_3\text{O}_4@\text{SiO}_2\text{-NP:C2}$ (b). The middle row shows TEM images of Fe_3O_4 (c) and $\text{Fe}_3\text{O}_4@\text{SiO}_2\text{-NP}$ (d). The bottom row shows EDS mapping (e) and TEM image (f) of $\text{Fe}_3\text{O}_4@\text{SiO}_2\text{-NP:C2}$.



with a sponge-like surface morphology alongside with a certain degree of aggregation. High-resolution TEM clearly demonstrated the crystalline structure of the iron-nanoparticles ($\text{Fe}_3\text{O}_4\text{-NP}$) with interplane distances of 0.11, 0.21 and 0.25 nm (Fig. 3c). These are in very good agreement with the XRD experimental results as well as with the reported XRD pattern for magnetite (ICDD 01-080-6402). TEM-EDS provided elemental composition identification of the silica coating as shown in the elemental distribution map in Fig. 3e. These results confirmed that the coating of the iron nanoparticles ($\text{Fe}_3\text{O}_4\text{-NP}$) with silica by ultrasonication was done successfully and that grafting of the C2 complex did not modify the surface morphology as well. TEM images, Fig. 3d and f, evidenced that the diameter of the nanoparticles was approximately 30 nm, while being coated with a layer of silica. TEM-EDS also confirmed the success of the grafting process with absence of induced changes in the $\text{Fe}_3\text{O}_4\text{@SiO}_2\text{-NP}$ morphology and micro-structure (Fig. 3d).

The particle size was also assessed through dynamic light scattering (DLS) measurements (Table S1, ESI†) in water at pH 7. Particle diameter of 85 and 91 nm for $\text{Fe}_3\text{O}_4\text{@SiO}_2\text{-NP}$ and $\text{Fe}_3\text{O}_4\text{@SiO}_2\text{-NP:C2}$, respectively, were measured by DLS. Results showed a particle size that is nearly three times larger than the TEM observation. This is corroborated by previous literature data and may arise from aggregation of the nanoparticles in the DLS measurements.⁴³ In addition, the ζ potential values measured for both $\text{Fe}_3\text{O}_4\text{@SiO}_2\text{-NP}$ and $\text{Fe}_3\text{O}_4\text{@SiO}_2\text{-NP:C2}$ were -38.91 and 43.17 mV, respectively. The former value reflects the surface covered by silanol groups, which may deprotonate and yield siloxane moieties with negative charges.⁴⁴ The latter indicates the presence of the Eu complex at the surface, which has an inherently positive charge due to the Eu^{3+} ion.

Synthesis and characterization of the silica nanoparticles

Silica nanoparticles ($\text{SiO}_2\text{-NP}$) were also synthesized (Scheme 1c) to evaluate the possible influence of the iron oxide core on both the Eu complex photoluminescent properties and on the cell viability studies, as will be discussed later in this work. The silica nanoparticles were synthesized by a co-precipitation method using tetraethylorthosilicate (TEOS), ammonia, Milli-Q water, and methanol as solvent.³⁷

The process of modification of the $\text{SiO}_2\text{-NP}$ surface followed the same procedure as for the $\text{Fe}_3\text{O}_4\text{@SiO}_2\text{-NP}$ (Scheme 1c). The Eu complex, C2, was directly grafted in a single step at the surface of the $\text{SiO}_2\text{-NP}$, yielding the $\text{SiO}_2\text{-NP:C2}$ nanomaterial.

Characterization of $\text{SiO}_2\text{-NP}$ by FTIR (Fig. S2b, ESI†) showed the characteristic band of $\nu\text{Si-O-Si}$ modes at 1060 cm^{-1} . This mode was predominant in the final $\text{SiO}_2\text{-NP:C2}$ counterpart, evidencing that the structure of the host material was not affected by the grafting procedure. The spectrum of $\text{SiO}_2\text{-NP:C2}$ also showed the presence of some characteristic bands arising from the surface-bound Eu complex. The characteristic bands identified were found at $3500\text{--}3300\text{ cm}^{-1}$ due to the $\nu\text{N-H}$ modes of the 3-aminopropyl ligand. Further characteristic bands at $1680\text{--}1610$ and at $1600\text{--}1500\text{ cm}^{-1}$ due to $\nu\text{C=N}$ and $\nu\text{C=C}_{\text{aromatic}}$ modes confirmed the presence of the *phen* aromatic moiety.

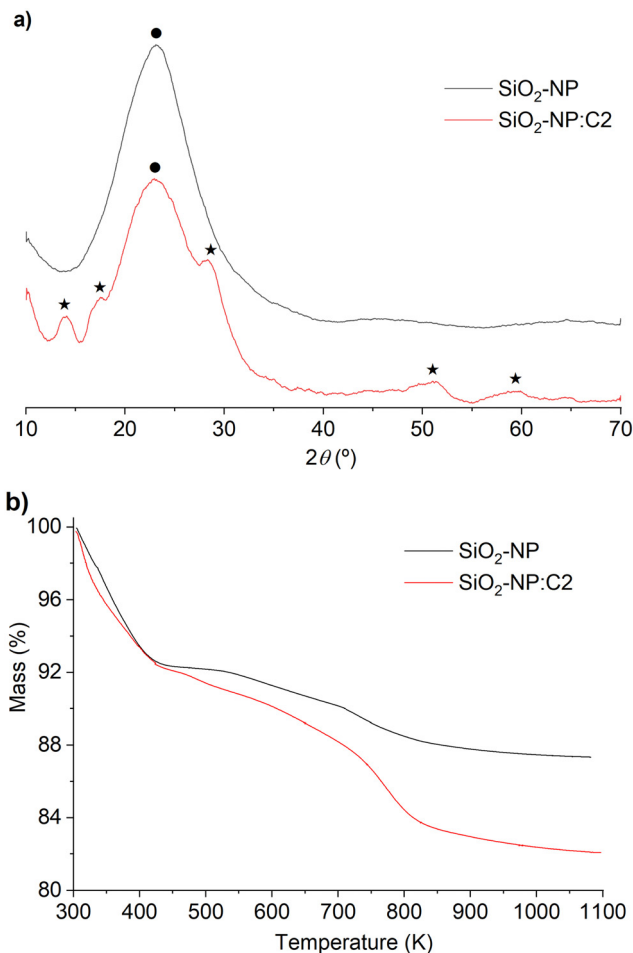


Fig. 4 X-Ray powder diffraction patterns of the silica nanoparticles ($\text{SiO}_2\text{-NP}$ and $\text{SiO}_2\text{-NP:C2}$) (a) and thermogravimetric analysis (TGA) of $\text{SiO}_2\text{-NP}$ and $\text{SiO}_2\text{-NP:C2}$ nanoparticles (b). The diffraction peaks marked with ● are due to silica, while those marked with ★ are due to the presence of the Eu complex.

The XRD patterns (Fig. 4a) of the $\text{SiO}_2\text{-NP}$ and $\text{SiO}_2\text{-NP:C2}$ nanoparticles showed a wide reflection typical of silica amorphous materials at $2\theta = 22.5^\circ$. The intensity of the peak decreased in the $\text{SiO}_2\text{-NP:C2}$ nanomaterial due to the presence of Eu, which also scatters X-rays.⁴² Additionally, the diffractogram of $\text{SiO}_2\text{-NP:C2}$ also displays extra diffraction peaks (★ in Fig. 4a), due to the presence of the Eu complex.

Similarly to the magnetic counterparts, thermogravimetric analysis (TGA) was also carried out to determine thermal decomposition profile of both $\text{SiO}_2\text{-NP}$ and $\text{SiO}_2\text{-NP:C2}$ nanomaterials.

Analysis of the thermogravimetric profile (Fig. 4b) of $\text{SiO}_2\text{-NP}$ an initial mass loss of 7.7% was observed in the 303–450 K temperature range, corresponding to surface adsorbed water and, eventually, some residual methanol solvent used in the synthesis. At higher temperatures, a single degradation step amounting to 5% was observed, which was mostly due to desorption of strongly bound water molecules and to some dehydroxylation processes at the surface. This is similar to what was observed and described earlier in this work for the $\text{Fe}_3\text{O}_4\text{@SiO}_2\text{-NP}$ nanomaterial.



The thermogravimetric profile of the $\text{SiO}_2\text{-NP:C2}$ showed the same two-step profile. The first degradation step was observed across roughly the same temperature range, 303–430 K as with pristine $\text{SiO}_2\text{-NP}$ counterpart, corresponding to a similar mass loss of 7.3%, accounting for adsorbed moisture and some residual methanol solvent. The following step, observed between 430 and 1100 K yielded an overall mass loss of 10.2%. Accounting for the 5% mass loss of the pristine $\text{SiO}_2\text{-NP}$, expected here as well, this yields a net loss of 5.2% due to the thermal degradation of the complex, which indicated a loading of 0.12 mmol g^{-1} . Elemental analysis showed an Eu content of 3.15%, yielding a loading of 0.21 mmol g^{-1} , showing a good agreement between both values. As mentioned earlier, the lower value obtained from TGA is due to the fact that Eu atoms will be part of the final mass, most probably in the form

of an oxide and, therefore, the loading value is not as accurate as that obtained from the Eu elemental analysis.

SEM and TEM were also carried out to characterize morphologically the $\text{SiO}_2\text{-NP}$ and $\text{SiO}_2\text{-NP:C2}$ nanomaterials. The SEM images of the pristine $\text{SiO}_2\text{-NP}$, Fig. 5a, showed the presence of spherical particles. Functionalization of the pristine nanoparticles, yielding $\text{SiO}_2\text{-NP:C2}$, induced little or no changes at the surface of the particles as evidenced in Fig. 5b, although a higher degree of agglomeration was observed.

The TEM images obtained for both $\text{SiO}_2\text{-NP}$ and $\text{SiO}_2\text{-NP:C2}$ nanomaterials, Fig. 5c and d, respectively, confirmed the observations made by SEM, although with more detail. TEM-EDS elemental ID and distribution confirmed the production of $\text{SiO}_2\text{-NP:C2}$ (Fig. 5e). Pristine $\text{SiO}_2\text{-NP}$ are around 30 nm in diameter though grafting of such material lead to larger $\text{SiO}_2\text{-}$

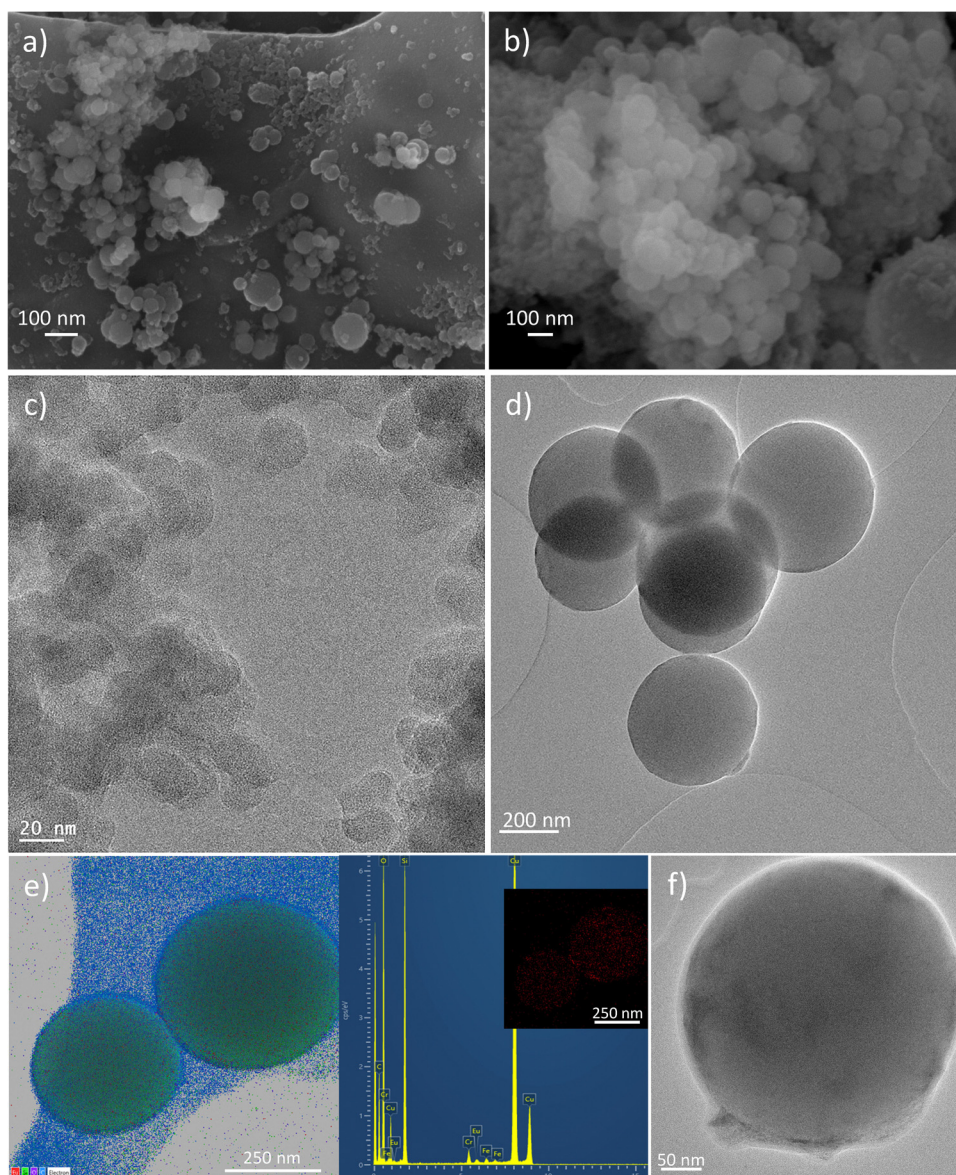


Fig. 5 The top row shows SEM images of SEM of $\text{SiO}_2\text{-NP}$ (a) and $\text{SiO}_2\text{-NP:C2}$ (b). The middle row shows the corresponding TEM images of $\text{SiO}_2\text{-NP}$ (c) and $\text{SiO}_2\text{-NP:C2}$ (d). The bottom row shows EDS mapping (e) and TEM image of $\text{SiO}_2\text{-NP:C2}$ (f).



NP:C2 particles, as shown in Fig. 5d and f. Nevertheless, one should bear in mind that the synthesis of iron nanoparticles with europium complex ($\text{Fe}_3\text{O}_4@\text{SiO}_2\text{-NP:C2}$) lead to similar morphology and diameter (around 30 nm) to those of pristine $\text{SiO}_2\text{-NP}$.

As previously, particle size was also assessed through DLS measurements (Table S1, ESI†) in water at pH 7. Particle diameter was found to be 73 and 77 nm for $\text{SiO}_2\text{-NP}$ and $\text{SiO}_2\text{-NP:C2}$, respectively, as measured by DLS. Compared to the sizes measured by TEM the values followed the same trend by being larger, most possibly due to particle aggregation in solution.⁴³ The measured ζ potential values for both $\text{SiO}_2\text{-NP}$ and $\text{SiO}_2\text{-NP:C2}$ were -40.64 and 46.31 mV, respectively. As discussed earlier in this work, the former value reflects the surface silanol groups, which may deprotonate and yield siloxane moieties with negative charges.⁴⁴ On the other hand, the latter is due to the presence of the Eu complex at the surface, which has an positive charge due to the Eu^{3+} ion.

Solid fluorescence studies

The excitation and emission spectra of the C2 complex were recorded at room temperature (Fig. S3, ESI†) for further comparison with the obtained spectra for $\text{SiO}_2\text{-NP:C2}$ and $\text{Fe}_3\text{O}_4@\text{SiO}_2\text{-NP:C2}$ nanomaterials. Fig. 6 shows the excitation (a, b) and emission (c, d) spectra of $\text{SiO}_2\text{-NP:C2}$ and $\text{Fe}_3\text{O}_4@\text{SiO}_2\text{-NP:C2}$ nanomaterials, respectively. The excitation spectra were obtained by monitoring the most intense europium(III) intra- $4f^6$ transition, $^5\text{D}_0 \rightarrow ^7\text{F}_2$, at 613 and 614 nm.

Overall, the excitation spectra (Fig. 6a and b) are both dominated by a broad band within different ranges (250–300 nm for $\text{Fe}_3\text{O}_4@\text{SiO}_2\text{-NP:C2}$ and 250–360 nm for $\text{SiO}_2\text{-NP:C2}$), assigned to the $\pi\text{-}\pi^*$ electronic transitions of the phenanthroline ligands.

The narrow lines characteristic of the energy levels of the Eu^{3+} ion corresponding to the intra- $4f^6$, $^7\text{F}_0 \rightarrow ^5\text{L}_6$, $^5\text{D}_{3-1}$ transitions were observed for the $\text{SiO}_2\text{-NP:C2}$ (Fig. 6a), showing almost the same pattern as observed for the C2 complex (Fig. S3, ESI†). The lower intensity relative to the band attributed to the excited states of the phenanthroline ligand indicates that the Eu^{3+} sensitization process is more efficient than direct excitation for intra- $4f^6$ levels.

The observed shift to shorter wavelengths (compared with the excitation spectrum of the C2 complex, Fig. S3, ESI†) as well as the decrease in the relative intensity of the intra- $4f^6$ lines could possibly be attributed to subtle changes in the structure of the Eu complex and the apparent beneficial effect that silica has on the sensitization process.

A complete disappearance of the narrow lines characteristic of the energy levels of the Eu^{3+} ion were observed for the excitation spectrum of $\text{Fe}_3\text{O}_4@\text{SiO}_2\text{-NP:C2}$ (Fig. 6b), suggested that the ligand \rightarrow metal energy transfer processes were extremely efficient in comparison with that found for both $\text{SiO}_2\text{-NP:C2}$ and C2 complex as confirmed by Fig. 7 when exposed to 365 nm UV light. It also showed that the $\text{Fe}_3\text{O}_4\text{-NP}$ core did not induce fluorescence quenching.

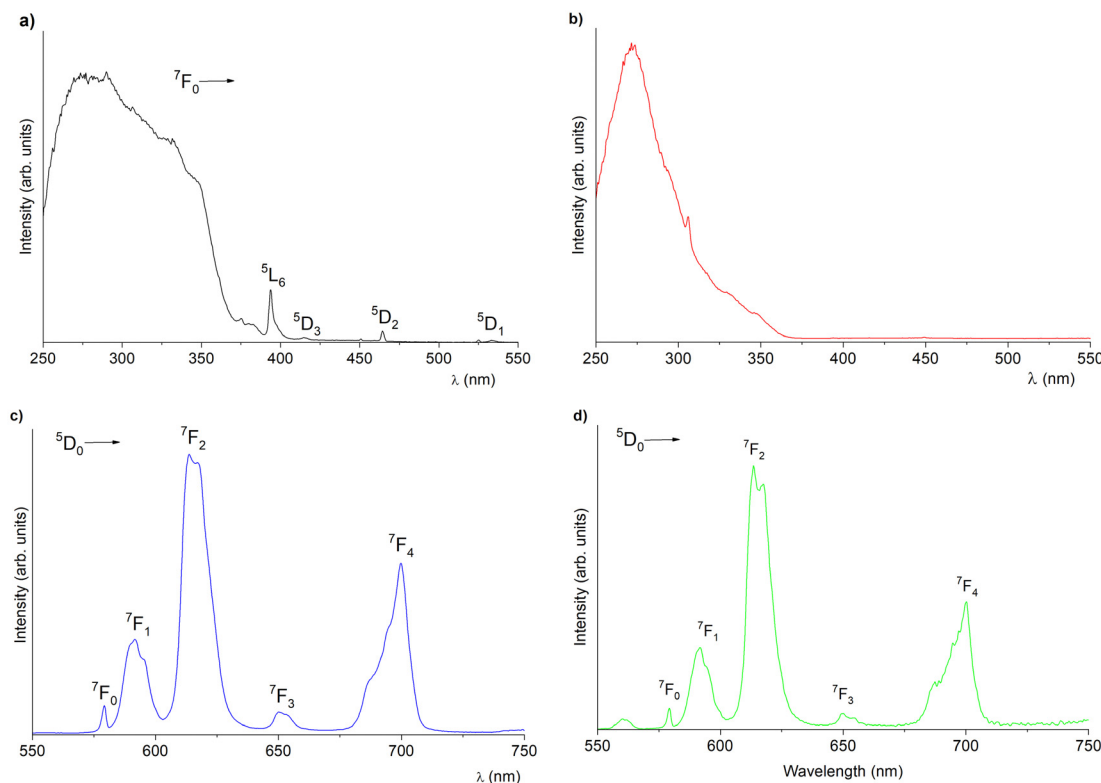


Fig. 6 Excitation spectra of $\text{SiO}_2\text{-NP:C2}$ (a) and of $\text{Fe}_3\text{O}_4@\text{SiO}_2\text{-NP:C2}$ (b) monitored at 614 and 613 nm, respectively. Emission spectra of $\text{SiO}_2\text{-NP:C2}$ (c) and of $\text{Fe}_3\text{O}_4@\text{SiO}_2\text{-NP:C2}$ (d). With excitation at 290 and 280 nm, respectively.



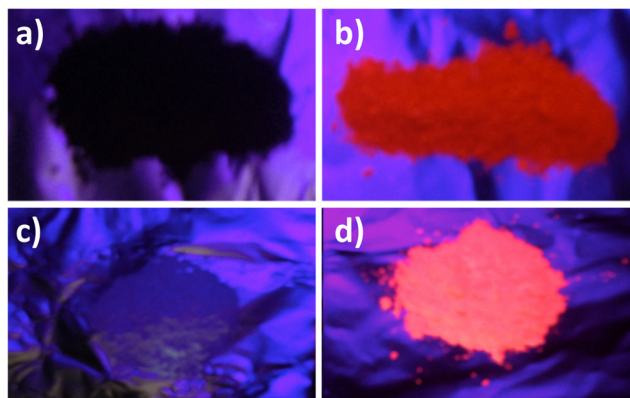


Fig. 7 Appearance of non-emissive SiO₂-NP (a) and Fe₃O₄@SiO₂-NP (c) and of emissive SiO₂-NP:C2 (b) and Fe₃O₄@SiO₂-NP:C2 (d) nanoparticles when irradiated by 365 nm UV light.

When excited at 290 and 280 nm, both SiO₂-NP:C2 (Fig. 6c) and Fe₃O₄@SiO₂-NP:C2 (Fig. 6d) emission spectra, measured at room temperature, showed narrow lines attributed to the transitions between the first excited state and the fundamental multiplet, $^5D_0 \rightarrow ^7F_{0-4}$ (as observed also for the C2 complex, Fig. S3, ESI[†]).

Due to the field of the ligands, an unfolding was evident for the $^5D_0 \rightarrow ^7F_{1-2}$ transitions, both present two Stark components.

This fact suggested that the Eu³⁺ ions occupy a position of low symmetry, without inversion center, according to the great intensity of the transition $^5D_0 \rightarrow ^7F_2$. Additionally, the presence of only a single line for the $^5D_0 \rightarrow ^7F_0$ transition in the emission spectrum of both SiO₂-NP:C2 and Fe₃O₄@SiO₂-NP:C2 (Fig. 6c and d) as well as in the emission spectrum of the C2 complex (Fig. S3, ESI[†]), were a strong indicator for the existence of a single coordination environment for europium ions. In addition, this also evidenced that the first Eu³⁺ coordination sphere in the C2 complex and in both the SiO₂-NP:C2 and Fe₃O₄@NP:C2 nanoparticles was identical. Furthermore, the ratio between the $^5D_0 \rightarrow ^7F_2$ and $^5D_0 \rightarrow ^7F_1$ transitions across all species, C2, SiO₂-NP:C2 and Fe₃O₄@SiO₂-NP:C2, was found to be constant, confirming the single coordination environment in all of them.

Cytotoxic activity tests *in vitro*

Studying cell viability or cytotoxic activity evidence whether a given material will be suitable to be used as a bioprobe. For that purpose, both the SiO₂-NP:C2 and Fe₃O₄@SiO₂-NP:C2 nanomaterials as well as the Eu complex were tested to assess their effects on HeLa (cervical cancer) and A549 (adenocarcinoma human alveolar basal epithelial cells) cell lines.

Determination of the cell viability was performed for Eu complex, pristine Fe₃O₄@SiO₂-NP and SiO₂-NP nanomaterials (Fig. S4, ESI[†]) and for the SiO₂-NP:C2 and Fe₃O₄@SiO₂-NP:C2

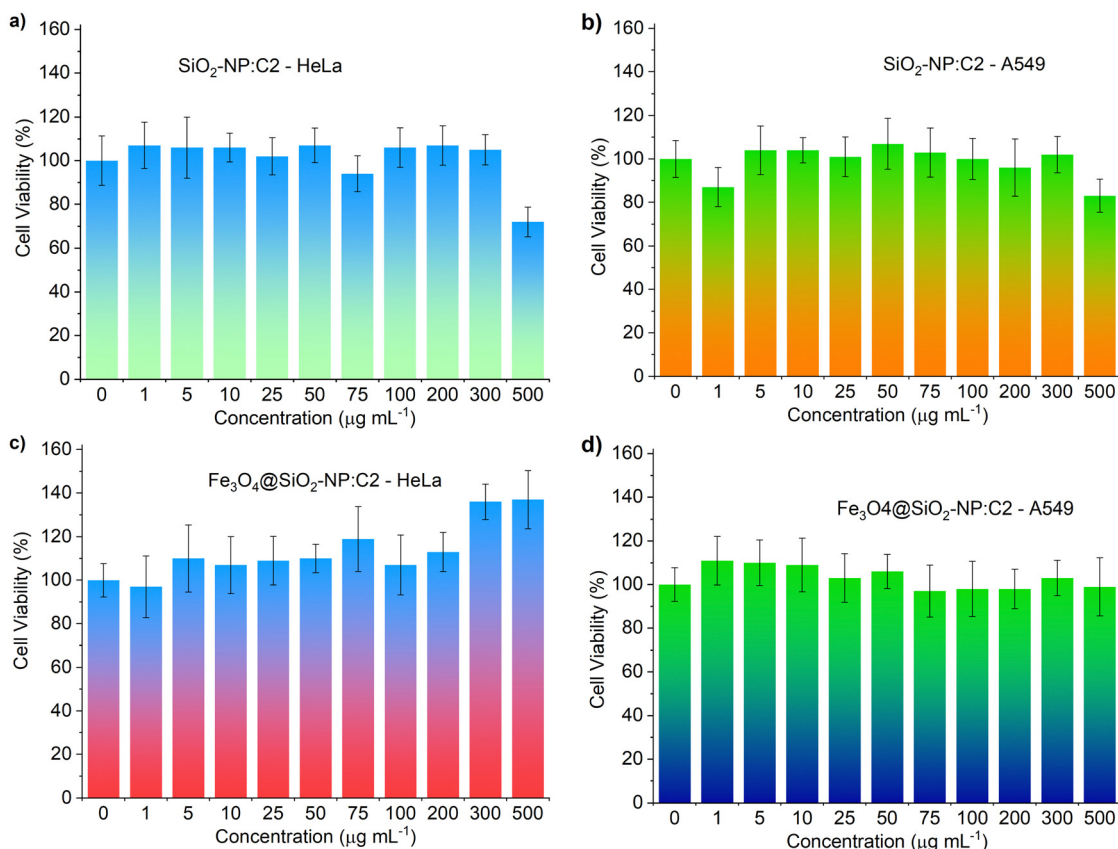


Fig. 8 Cell viability tests of SiO₂-NP:C2 (a, b) and Fe₃O₄@SiO₂-NP:C2 (c, d) on HeLa (cervical cancer) (a, c) and A549 (adenocarcinoma human alveolar basal epithelial cells) (b, d) cell lines.



composite counterparts (Fig. 8). For that purpose, the cell lines were incubated with different concentrations of a given sample (1, 5, 10, 25, 50, 75, 100, 200, 300 and 500 $\mu\text{g mL}^{-1}$) for 48 h and then the MTT assay was performed.⁴⁵

The results of the cell viability test for the Eu complex (Fig. S4; tested at 1, 5, 10, 25, 50, 75, 100, 200 μM , ESI†) showed some cytotoxicity at concentrations of 75 μM and above for the HeLa cells and of at least 100 μM for the A549 cells (Fig. S4, ESI†). On the other hand, the pristine materials, $\text{SiO}_2\text{-NP}$ and $\text{Fe}_3\text{O}_4@\text{SiO}_2\text{-NP}$, showed no cytotoxic effects in general (Fig. S4, ESI†). The exception was $\text{SiO}_2\text{-NP}$, which for the highest concentration (500 $\mu\text{g mL}^{-1}$) evidenced some degree of cytotoxicity with a higher impact on HeLa cells. Results from the cell viability tests of the $\text{SiO}_2\text{-NP:C2}$ and $\text{Fe}_3\text{O}_4@\text{SiO}_2\text{-NP:C2}$ derivatized nanomaterials are shown in Fig. 8. According to the data shown in Fig. 8 the nanomaterials did not show any cytotoxic effects against both cell lines aligning with the results of the pristine nanomaterials. In fact, this is a somewhat surprising, yet welcome finding as their behavior was more similar to the parent nanomaterials than to that was evidenced by the C2 complex. Even at the highest concentration (500 $\mu\text{g mL}^{-1}$) there was only a slight cytotoxic effect found for $\text{SiO}_2\text{-NP:C2}$ in both cell lines.

According to the above results, determination of the 50% inhibitory concentration value of cell growth (IC_{50}) could not be done for any of the tests, since all tested samples were mostly harmless for both cell lines. These results were different from those recently reported by us.³⁸ While in that work the aim was to develop dual modality probes, for both imaging and cell killing, the goal of the present work was to develop solely bioprobes.

Conclusion

In the present research, a visible-light-excitable, phenanthroline Eu complex with an aminopropyltrimethoxysilane (*aptms*) ligand was synthesized. The *aptms* molecule has a functional NH_2 group prone to coordination to the Eu core, while the siloxane moiety allowed grafting by covalent bonding of the Eu complex at the surface of both magnetic silica-coated iron oxide and neat silica nanoparticles.

The silica and magnetic iron oxide nanoparticles derivatized with a europium complex synthesized in this work were structurally characterized successfully.

Synthesized iron oxide magnetic nanoparticles were 30 nm in diameter, and monodispersed, when dispersed in water, while retaining their excellent luminescence properties of the grafted Eu complex. The silica nanoparticles modified with the Eu complex presented an apparent higher degree of aggregation and diameter around 150 nm. Yet, the one-step preparation of the nanocomposite $\text{Fe}_3\text{O}_4@\text{SiO}_2\text{-NP:C2}$ clearly lead to silica nanoparticles around 30 nm in diameter.

In addition, their photophysical properties evidenced that the host nanoparticles did not quench europium fluorescence emission. Furthermore, the emission spectra of both Eu

derivatized nanoparticles also showed that the nature of transitions was somewhat different, which is an outstanding finding.

Cytotoxicity testing to assess whether these nanomaterials could be hypothetically used as bioprobes evidenced excellent cell viability even at extremely elevated concentrations as high as 500 $\mu\text{g mL}^{-1}$. These results confirmed the potential role of these new nanomaterials to be used as bioprobes in cell imaging without major cytotoxicity issues. Furthermore, the fact that the iron oxide nanoparticles are paramagnetic could also render them application as magnetic resonance imaging (MRI) contrast agents.

Author contributions

C. D. N: conception, design and data curation of the work; C. D. N, P. D. V., M. M. N., A. V. G.: main manuscript text writing; P. D. V., A. V. G.: main figure preparation; I. M.: synthesis of samples and characterization. A. V. G.: Electron microscopy; M. M. N.: luminescence data acquisition; All authors reviewed the manuscript.

Conflicts of interest

There are no conflicts to declare.

Acknowledgements

This work was supported by Fundação para a Ciência e Tecnologia – Ministério da Ciência e Tecnologia e Ensino Superior (FCT-MCTES, Portugal), projects UIDB/00100/2020, UIDP/00100/2020 and LA/P/0056/2020. This work was developed within the scope of the project CICECO-Aveiro Institute of Materials, UIDB/50011/2020, UIDP/50011/2020 & LA/P/0006/2020, financed by national funds through the FCT/MCTES (PIDDAC).

References

- 1 *The Chemistry of Contrast Agents in Medical Magnetic Resonance Imaging*, ed. A. Merbach, L. Helm and É. Tóth, Wiley, 2013.
- 2 *Fluorescent Materials for Cell Imaging*, ed. F.-G. Wu, Springer, Singapore, 2020.
- 3 S. A. Wickline and G. M. Lanza, *J. Cell. Biochem.*, 2002, **87**, 90–97.
- 4 J. P. Kehrer, *Toxicology*, 2000, **149**, 43–50.
- 5 Y.-X. J. Wang, S. M. Hussain and G. P. Krestin, *Eur. Radiol.*, 2001, **11**, 2319–2331.
- 6 A. G. Roca, M. P. Morales, K. O'Grady and C. J. Serna, *Nanotechnology*, 2006, **17**, 2783–2788.
- 7 H. Nakamura, N. Ito, F. Kotake, Y. Mizokami and T. Matsuoka, *J. Gastroenterol.*, 2000, **35**, 849–855.
- 8 J. S. Weinstein, C. G. Varallyay, E. Dosa, S. Gahramanov, B. Hamilton, W. D. Rooney, L. L. Muldoon and E. A. Neuwelt, *J. Cereb. Blood Flow Metab.*, 2010, **30**, 15–35.
- 9 T. Atabaev, J. Lee, Y. Shin, D.-W. Han, K. Choo, U. Jeon, J. Hwang, J. Yeom, H.-K. Kim and Y.-H. Hwang, *Nanomaterials*, 2017, **7**, 35.



- 10 R. Subbiah, M. Veerapandian and K. S. Yun, *Curr. Med. Chem.*, 2010, **17**, 4559–4577.
- 11 J.-H. Park, L. Gu, G. von Maltzahn, E. Ruoslahti, S. N. Bhatia and M. J. Sailor, *Nat. Mater.*, 2009, **8**, 331–336.
- 12 S.-J. Yu, M.-W. Kang, H.-C. Chang, K.-M. Chen and Y.-C. Yu, *J. Am. Chem. Soc.*, 2005, **127**, 17604–17605.
- 13 L. Gu, D. J. Hall, Z. Qin, E. Anglin, J. Joo, D. J. Mooney, S. B. Howell and M. J. Sailor, *Nat. Commun.*, 2013, **4**, 2326.
- 14 F. Erogbogbo, K.-T. Yong, I. Roy, R. Hu, W.-C. Law, W. Zhao, H. Ding, F. Wu, R. Kumar, M. T. Swihart and P. N. Prasad, *ACS Nano*, 2011, **5**, 413–423.
- 15 L. M. Jurkić, I. Cepanec, S. K. Pavelić and K. Pavelić, *Nutr. Metab.*, 2013, **10**, 2.
- 16 H. Jaganathan and B. Godin, *Adv. Drug Delivery Rev.*, 2012, **64**, 1800–1819.
- 17 A. Bitar, N. M. Ahmad, H. Fessi and A. Elaissari, *Drug Discovery Today*, 2012, **17**, 1147–1154.
- 18 X. Zhao, L. R. Hilliard, S. J. Mechery, Y. Wang, R. P. Bagwe, S. Jin and W. Tan, *Proc. Natl. Acad. Sci. U. S. A.*, 2004, **101**, 15027–15032.
- 19 M. Arruebo, R. Fernández-Pacheco, M. R. Ibarra and J. Santamaría, *Nano Today*, 2007, **2**, 22–32.
- 20 D. Svehkarev and A. M. Mohs, *Curr. Med. Chem.*, 2019, **26**, 4042–4064.
- 21 N. Yin, P. Wu, G. Liang and W. Cheng, *Appl. Phys. A: Mater. Sci. Process.*, 2016, **122**, 243.
- 22 W. Cheng, H. Chen, C. Liu, C. Ji, G. Ma and M. Yin, *View*, 2020, **1**, 20200055.
- 23 E. C. Jensen, *Anat. Rec.*, 2012, **295**, 2031–2036.
- 24 B. Francis, B. Neuhaus, M. L. P. Reddy, M. Epple and C. Janiak, *Eur. J. Inorg. Chem.*, 2017, 3205–3213.
- 25 C. Liu, Y. Hou and M. Gao, *Adv. Mater.*, 2014, **26**, 6922–6932.
- 26 S. S. Syamchand and G. Sony, *J. Lumin.*, 2015, **165**, 190–215.
- 27 K. Szyszka, S. Targonska, M. Gazinska, K. Szustakiewicz and R. J. Wiglus, *Nanomaterials*, 2019, **9**, 1146.
- 28 K. R. M. da Silva, C. M. S. Calado, T. V. dos Santos, T. de, O. Sales, R. da, S. Viana, U. R. Silva, R. A. S. Ferreira, L. D. Carlos and C. D. A. E. S. Barbosa, *J. Mater. Chem. C*, 2022, **10**, 11614–11624.
- 29 T. K. L. Rezende, H. P. Barbosa, L. F. dos Santos, K. D. O. Lima, P. Alves de Matos, T. M. Tsubone, R. R. Gonçalves and J. L. Ferrari, *Front. Chem.*, 2022, **10**, 1035449.
- 30 V. Gubala, G. Giovannini, F. Kunc, M. P. Monopoli and C. J. Moore, *Cancer Nanotechnol.*, 2020, **11**, 1.
- 31 C. P. Montgomery, B. S. Murray, E. J. New, R. Pal and D. Parker, *Acc. Chem. Res.*, 2009, **42**, 925–937.
- 32 M. Mahmoudi, H. Hosseinkhani, M. Hosseinkhani, S. Boutry, A. Simchi, W. S. Journeay, K. Subramani and S. Laurent, *Chem. Rev.*, 2011, **111**, 253–280.
- 33 C. Wang, L. Cheng and Z. Liu, *Biomaterials*, 2011, **32**, 1110–1120.
- 34 S. L. C. Pinho, H. Faneca, C. F. G. C. Geraldés, J. Rocha, L. D. Carlos and M. Delville, *Eur. J. Inorg. Chem.*, 2012, 2828–2837.
- 35 S. Shylesh, L. Wang and W. R. Thiel, *Adv. Synth. Catal.*, 2010, **352**, 425–432.
- 36 X. Sun, F. Liu, L. Sun, Q. Wang and Y. Ding, *J. Inorg. Organomet. Polym. Mater.*, 2012, **22**, 311–315.
- 37 J.-H. Lim, S.-W. Ha and J.-K. Lee, *Bull. Korean Chem. Soc.*, 2012, **33**, 1067–1070.
- 38 M. R. Felício, P. D. Vaz, C. D. Nunes and M. M. Nolasco, *New J. Chem.*, 2022, **46**, 21311–21323.
- 39 J. Lhoste, N. Henry, T. Loiseau and F. Abraham, *Polyhedron*, 2011, **30**, 1289–1294.
- 40 I. Chourpa, L. Douziech-Eyrolles, L. Ngaboni-Okassa, J.-F. Fouquenot, S. Cohen-Jonathan, M. Soucé, H. Marchais and P. Dubois, *Analyst*, 2005, **130**, 1395.
- 41 C. I. Fernandes, M. D. Carvalho, L. P. Ferreira, C. D. Nunes and P. D. Vaz, *J. Organomet. Chem.*, 2014, **760**, 2–10.
- 42 C. I. Fernandes, G. B. G. Stenning, J. D. Taylor, C. D. Nunes and P. D. Vaz, *Adv. Synth. Catal.*, 2015, **357**, 3127–3140.
- 43 T. G. F. Souza, V. S. T. Ciminelli and N. D. S. Mohallem, *J. Phys.: Conf. Ser.*, 2016, **733**, 012039.
- 44 N. Chekalil, M. Tarhini, A. Elaissari and S. Saïdi-Besbes, *Res. Chem. Intermed.*, 2019, **45**, 4847–4861.
- 45 T. Mosmann, *J. Immunol. Methods*, 1983, **65**, 55–63.

